

Nonstatistical Dissociation Dynamics of Nitroaromatic Chromophores

Published as part of *The Journal of Physical Chemistry virtual special issue "Pacific Conference on Spectroscopy and Dynamics"*.

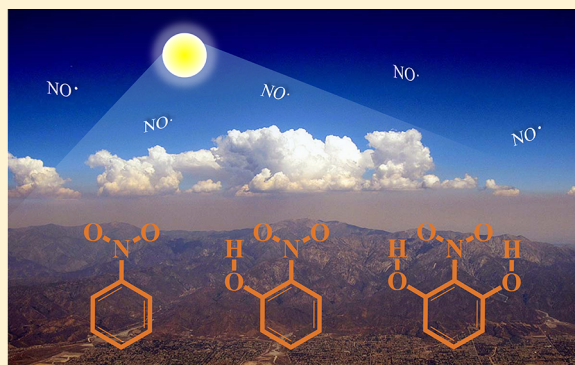
K. Jacob Blackshaw,[†] Belinda I. Ortega,[‡] Naa-Kwarley Quarley,[†] Wade E. Fritzeen,[†] Robert T. Korb,[†] Annalise K. Ajmani,[†] Lehman Montgomery,[†] Marcus Marracci,[‡] Geronimo Gudino Vanegas,[‡] John Galvan,[‡] Zach Sarvas,[‡] Andrew S. Petit,^{*,‡} and Nathanael M. Kidwell^{*,†}

[†]Department of Chemistry, The College of William and Mary, Williamsburg, Virginia 23187-8795, United States

[‡]Department of Chemistry and Biochemistry, California State University—Fullerton, Fullerton, California 92834-6866, United States

S Supporting Information

ABSTRACT: Organic carbon in the atmosphere is emitted from biogenic and anthropogenic sources and plays a key role in atmospheric chemistry, air quality, and climate. Recent studies have identified several of the major nitroaromatic chromophores embedded in organic "brown carbon" (BrC) aerosols. Indeed, nitroaromatic chromophores are responsible for the enhanced solar absorption of BrC aerosols, extending into the near UV (300–400 nm) and visible regions. Furthermore, BrC chromophores serve as temporary reservoirs of important oxidizing intermediates including hydroxyl (OH) and nitric oxide (NO) radicals that are released upon electronic excitation. The present work represents the first study of the 355 nm photolysis of known BrC chromophores *ortho*-nitrophenol and 2-nitroresorcinol, as well as the prototypical nitroaromatic, nitrobenzene. Experiments are carried out in a pulsed supersonic jet expansion with velocity map imaging of NO $X^2\Pi$ ($\nu'' = 0, J''$) fragments to report on the photodissociation dynamics. The total kinetic energy release (TKER) distributions and the NO $X^2\Pi$ ($\nu'' = 0, J''$) product state distributions deviate significantly from Prior simulations, indicating that energy is partitioned nonstatistically following dissociation. Experiments are conducted in tandem with complementary calculations using multireference Møller–Plesset second-order perturbation theory (MRMP2) for stationary points obtained by using multiconfiguration self-consistent field (MCSCF) with an aug-cc-pVDZ basis on the ground and lowest energy triplet electronic states. Furthermore, insights into the partitioning of energy upon photodissociation are achieved by using relaxed scans at the MCSCF/aug-cc-pVDZ level of theory. As a whole, the results suggest that upon excitation to S_1 , all three nitroaromatics share a common overall mechanism for NO production involving isomerization of the nitro group, nonradiative relaxation to S_0 , and dissociation to form rotationally hot NO.



1. INTRODUCTION

The atmosphere has experienced an unprecedented transformation in its chemical composition due to anthropogenic emissions from hydrocarbon fuels, biomass burning, and the fast-expanding list of biofuels. This presents a challenge to the scientific community seeking to provide a molecular-scale understanding of their impact on the atmosphere. In pursuit of this goal, global models necessarily face a daunting task as they strive to incorporate the vast array of chemical reactions. The increased number of sources of volatile organic compounds yields many routes to the formation of aerosols, which have profound effects on atmospheric chemistry, air quality, and climate.^{1,2}

The interaction of solar radiation with aerosols has a significant, yet not entirely understood, impact on the Earth's climate, in which aerosols may scatter (cooling effect) or absorb (warming effect) incoming light.² A particular class of organic aerosols referred to as "brown carbon" (BrC) due to their color are ubiquitous in urban and rural atmospheres where they are formed primarily from biomass burning and secondarily from the oxidation of anthropogenic aromatics and alkenes.^{3–8} The ability of aerosol particles to scatter light is well established. However, recent work has demonstrated that

Received: March 12, 2019

Revised: April 29, 2019

Published: April 30, 2019

BrC aerosol particles can also strongly absorb visible and ultraviolet (UV) light. Indeed, several of the major light-absorbing nitroaromatic chromophores responsible for the enhanced light absorption properties of BrC aerosol particles were recently identified.^{3,4,8} The wide array of BrC chromophores have relatively high absorption coefficients in the solar spectral window^{9–11} that cause BrC aerosol particles to cool the atmosphere less compared to the assumption that they are purely scattering.^{6,12}

Prototypical molecules such as nitrobenzene, *o*-nitrophenol, and 2-nitroresorcinol (the focus of the present study) also exist as isolated molecules in the atmosphere. There is significant overlap between the absorption spectra of nitroaromatics with the actinic solar flux in the visible and UV regions. Figure 1

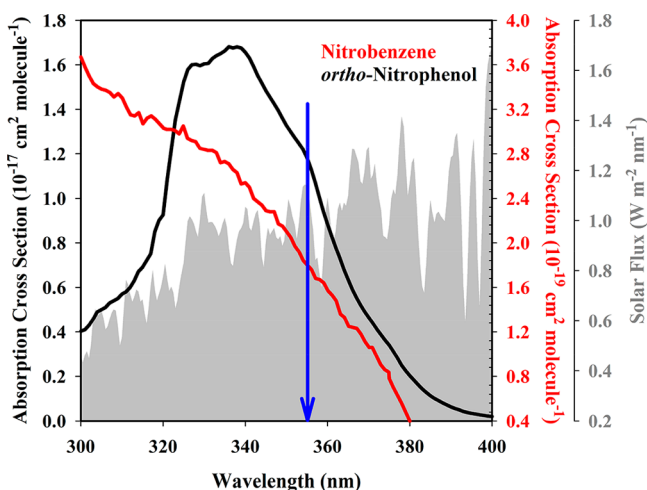


Figure 1. Absorption spectra of nitrobenzene (red trace) and *o*-nitrophenol (black trace) across the 300–400 nm range^{10,11} overlaid with the AM1.5 solar flux spectrum (gray shaded). The 355 nm photolysis wavelength used in the current study is denoted with a blue arrow. The corresponding gas phase absorption spectrum for 2-nitroresorcinol is not available in the literature, but its absorption spectrum in acetonitrile is reported in the [Supporting Information](#).

shows the gas phase absorption cross sections of nitrobenzene and *o*-nitrophenol across the 300–400 nm range.^{10,11} Since there is no corresponding spectrum for 2-nitroresorcinol available in the literature, we report the UV/visible spectra of *o*-nitrophenol and 2-nitroresorcinol dissolved in acetonitrile in the [Supporting Information](#). The UV/visible spectrum of *o*-nitrophenol exhibits an approximately 15 nm solvatochromic shift to the red relative to the gas phase absorption cross section spectrum shown in Figure 1. This magnitude of solvatochromic shift is consistent with the solvent weakly perturbing the electronic states of *o*-nitrophenol. Therefore, the weakly interacting solvent does not appreciably perturb the UV/visible spectra compared to the case for the gas phase. The UV/visible spectrum of 2-nitroresorcinol is red-shifted by approximately 50 nm relative to *o*-nitrophenol and will therefore overlap more strongly with incoming solar radiation. Nitroaromatics have central roles in the troposphere as temporary reservoirs of hydroxyl (OH) radical, nitric oxide (NO) radical, nitrogen dioxide (NO₂), and oxygen (O) atom photoproducts that are rapidly released upon electronic excitation. Indeed, OH and NO radicals are important atmospheric oxidizing intermediates, requiring knowledge of their sources and sinks.^{13,14}

Previous experimental and theoretical studies have shed light on the spectroscopy and dynamics of nitrobenzene. Galloway and co-workers employed 125 nm VUV ionization coupled with UV excitation of nitrobenzene from 220–320 nm to characterize the primary photodissociation products and energy partitioning to kinetic energy and cofragment internal energy.^{15,16} Using multimass ion imaging to measure the fragment kinetic energies, Lin et al. determined that the NO translational energy distributions are bimodal for nitrobenzene photolysis at 193, 248, and 266 nm.¹⁷ More recently, the Suits and Lin groups revealed that at 226 nm photolysis, the faster component in the bimodal NO translational distribution arises from contributions due to dissociation on the T₁ triplet state, whereas the slower component stems primarily from dissociation on the ground state, possibly through a roaming mechanism.¹⁸

The photochemistry of *o*-nitrophenol has also been previously explored in a number of studies. Sangwan and Zhu concluded that photolysis of *o*-nitrophenol in the near-UV primarily generated OH and HONO radicals, along with formation of NO.¹⁰ The photochemical dynamics of *o*-nitrophenol have been studied as well.^{19–21} Nascent OH radicals detected with laser-induced fluorescence from dissociation of *o*-nitrophenol from 361–390 nm were revealed to be nonstatistically formed in the vibrational $\nu'' = 0$ state and relatively low rotational J'' states.¹⁹ Using velocity map imaging (VMI) of hydrogen (H) atom fragments from dissociation of *o*-nitrophenol at 243 nm, Grygoryeva et al. concluded that fast internal conversion to the ground electronic state was responsible for the appearance of slow, statistical H atom fragments.²⁰ Finally, the ultrafast dynamics of *o*-nitrophenol were investigated by Ernst and co-workers on the first excited singlet state (S₁) with time-resolved photoelectron spectroscopy and quantum chemical calculations.²¹ The authors provided evidence for subpicosecond internal conversion to the ground state, in addition to a competitive intersystem crossing pathway on the triplet state manifold, which also ultimately leads back to the electronic ground state.

Theoretical calculations of the geometries and energetics in the ground state and in the singlet and triplet excited states of nitrobenzene and *o*-nitrophenol have been previously conducted by using high-level methods.^{22–27} Mewes et al. and Giussani et al. used multireference approaches to map out the internal conversion and intersystem crossing pathways associated with rapid nonradiative relaxation from the S₁ to the S₀ electronic states of nitrobenzene.^{25,27} While these studies primarily focused on nonisomerization processes, Giussani and Worth did describe a pathway from the nitrobenzene minimum energy structure on T₁ to phenyl nitrite on S₀.²⁵ Xu et al. used multireference methods to identify pathways for the rapid electronic relaxation of *o*-nitrophenol as well as for proton transfer between the nitro and hydroxyl groups.²² Furthermore, quantum chemical and theoretical kinetic studies were carried out by Vereecken et al.²⁶ for *o*-nitrophenol decomposition to atomic and molecular fragments on the S₀ and T₁ potential energy surfaces, showing that OH and NO radicals were the dominant degradation products.

The present work represents the first investigation of the 355 nm photodissociation dynamics of nitrobenzene, *o*-nitrophenol, and 2-nitroresorcinol using VMI along with characterization of the NO product state distributions. Despite 2-nitroresorcinol resembling more typical BrC chromophores,

there are no previous studies on its photodissociation. Multireference calculations are carried out in tandem to obtain physical insights into the photodissociation dynamics. In a combined experimental and theoretical investigation, a molecular-level understanding of the nonstatistical dissociation mechanisms for nitrobenzene, *o*-nitrophenol, and 2-nitroresorcinol is discussed.

2. EXPERIMENT

The UV photolysis dynamics of nitrobenzene, *o*-nitrophenol, and 2-nitroresorcinol were recorded under isolated-molecule conditions in a free-jet VMI apparatus that has been previously described in detail.²⁸ In separate experiments, the vapor of nitrobenzene, *o*-nitrophenol, or 2-nitroresorcinol is entrained in ~ 1 bar of argon by sufficiently heating the sample reservoir to 50 °C. Subsequently, a pulsed valve (1 mm, Parker General Valve Series 9) is used to form a supersonic jet expansion where collisional cooling occurs for the species of interest (rotational temperature ~ 10 K), which is interrogated downstream.

In the laser interaction region, photolysis is induced with 355 nm radiation generated from the third harmonic output of a Nd:YAG laser (Continuum Surelite II-10) operating at 5 Hz. A linear response in NO product formation and photolysis power for all experiments was ensured to minimize multiphoton effects. Furthermore, the 355 nm photolysis laser polarization was set parallel to the plane of the detector. Following a 50 ns time delay, a counterpropagating UV probe laser operating at 10 Hz is spatially overlapped with the photolysis laser to state-selectively ionize NO products by using a 1 + 1 resonance-enhanced multiphoton ionization (REMPI) scheme via the NO $\gamma(0,0)$ band of the $A^2\Sigma^+ \leftarrow X^2\Pi$ transition. The probe wavelengths are obtained by frequency-tripling the output of a Nd:YAG dye laser (Radiant Dyes, NarrowScan) with BBO crystals. The laser wavelengths are calibrated with a wavemeter (Coherent WaveMaster) and compared to the LIFBASE program results.²⁹ The probe laser power was reduced to ~ 100 $\mu\text{J}/\text{pulse}$ to reduce photodissociation of the precursor molecules.

After photodissociation, NO^+ are extracted by a stack of ion optics through a time-of-flight tube and velocity focused to impact a 40 mm microchannel plate (MCP) detector. The MCP is coupled to a fast phosphor screen that is electronically gated for NO^+ . Two-dimensional NO^+ ion images are captured with a CCD camera, and the acquisition is carried out by using a LabVIEW program. The experimental velocity resolution is approximately 5%, which was determined via O_2 photodissociation at 226 nm to O atoms that were detected by using 2 + 1 REMPI. In order to quantify the angular and velocity distributions, the ion images are reconstructed by using the pBASEX software.³⁰ The NO product state distribution from 355 nm photolysis of nitrobenzene, *o*-nitrophenol, or 2-nitroresorcinol is collected by scanning the probe laser on well-defined NO REMPI transitions and monitoring the enhanced ion signal. Ion images and product state distributions are recorded with active baseline subtraction to remove background signal.

3. THEORETICAL CALCULATIONS

Stationary points on the ground-state singlet (S_0) and lowest energy triplet (T_1) potential energy surfaces (PESs) were obtained by using the multiconfiguration self-consistent field

method (MCSCF) with an aug-cc-pVDZ basis and full configuration interaction within the active space.^{31,32} A more complete treatment of electron correlation at the optimized geometries was obtained by using multireference Møller–Plesset second-order perturbation theory (MRMPT2).³³ For nitrobenzene and *o*-nitrophenol, the chosen active space included the complete set of π molecular orbitals as well as those molecular orbitals with large amplitude on the NO_2 group and significant p-character. For 2-nitroresorcinol, the two π molecular orbitals consisting primarily of oxygen p-orbitals from the two hydroxyl groups were excluded from the active space. For nitrobenzene, the geometry optimizations were performed with an active space consisting of 14 electrons in 11 orbitals (14,11) while the active space for the MRMPT2 calculations was slightly larger at (16,13). For *o*-nitrophenol and 2-nitroresorcinol, both the geometry optimizations and MRMPT2 calculations used an (18,14) active space. Representative active spaces are summarized in the [Supporting Information](#). These calculations were performed by using the GAMESS software package and analyzed by using wxMacMolPlt.^{34–36}

It is worth noting that, particularly for the triplet stationary points, multireference methods were necessary to achieve an accurate PES. Analysis of the leading T_1 amplitudes from restricted open-shell CCSD(T)/cc-pVTZ calculations indicated significant multireference character at some of the triplet stationary points. Furthermore, geometry optimizations performed by using DFT at the $\omega\text{B97X-D}/6-311+\text{G}(3\text{df},2\text{p})$ level of theory predicted stationary point structures that were not replicable in subsequent MCSCF geometry optimizations.

For all parent molecules, relaxed scans along the O–NO dissociation coordinate were obtained by performing a series of constrained geometry optimization calculations at fixed O–NO bond lengths. For nitrobenzene and 2-nitroresorcinol, these calculations were performed at the (18,14) MCSCF/aug-cc-pVDZ level of theory while for *o*-nitrophenol, the calculations were performed by using (16,13) MCSCF/aug-cc-pVDZ. The chosen active spaces included π molecular orbitals as well as molecular orbitals with significant bonding or antibonding character around the O–NO bond that is breaking in the scan. At each of the optimized geometries, the individual dipole moments of the NO and aromatic cofragments were obtained at the restricted open-shell Møller–Plesset second-order perturbation theory (RO-MP2/aug-cc-pVDZ) level of theory. These calculations included the basis functions of the other fragment centered on ghost atoms. The fragment dipole moment calculations were performed by using Q-Chem 5.1.³⁷

Optimized geometries and harmonic vibrational frequencies of the phenoxy and hydroxyphenoxy radicals were obtained by using equation-of-motion ionization potential coupled cluster singles and doubles (EOM-IP-CCSD) level of theory using a cc-pVDZ basis.³⁸ The leading T_1 and T_2 amplitudes for both radicals do not suggest significant multireference character to the ground state wave function. Anharmonic vibrational frequencies of all three aromatic cofragments were separately obtained by using vibrational second-order perturbation theory (VPT2) at the M06-2X/6-311G(2df,2pd) level of theory.^{39,40} As shown in the [Supporting Information](#), these two methods yield similar vibrational frequencies phenoxy and hydroxyphenoxy. The EOM-IP-CCSD calculations were performed by using Q-Chem 5.1 while the anharmonic vibrational frequencies were obtained by using Gaussian 09.^{37,41}

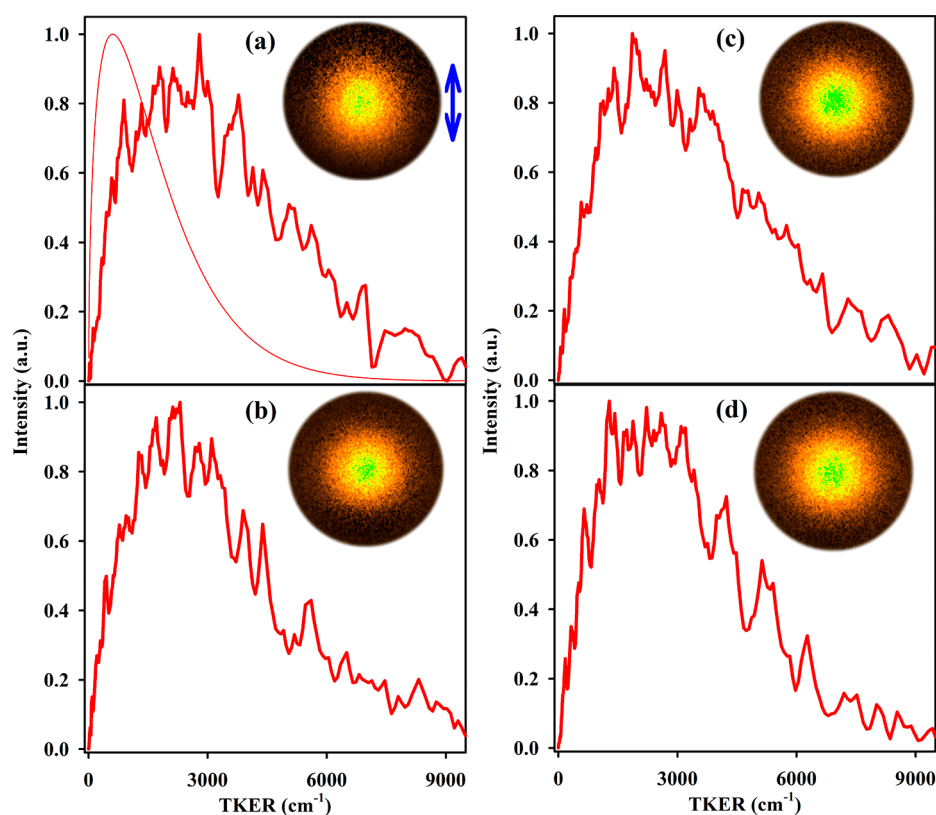


Figure 2. Velocity map ion images of NO products and total kinetic energy release (TKER) to NO ($\nu'' = 0$) and phenoxy products (red bold traces) recorded by using the (a) $Q_1(J''=20.5)$, (b) $R_1(J''=20.5)$, (c) $Q_1(J''=30.5)$, and (d) $R_1(J''=30.5)$ transitions following 355 nm photolysis of nitrobenzene using vertical polarization (blue arrow). The statistical Prior distribution (nonbold trace) is superimposed over the experimental results in the upper left panel.

4. RESULTS

Shown as insets in Figures 2–4 are the ion images collected while probing the NO $X^2\Pi_{1/2}$ ($\nu'' = 0, J''$) rotational states by using the Q_1 and R_1 lines. The polarization of the 355 nm pump laser is kept parallel to the detector (blue arrow). All other NO product rotational states displayed similar ion image results. The excited spin–orbit state ($^2\Pi_{3/2}$) was not examined in detail. The isotropic NO ion images indicate that the parent nitroaromatic molecules dissociate on a slower time scale than their respective rotational period ($\tau \geq 9$ –11 ps), on the basis of rotational constants from the literature and calculations.^{42,43}

Using linearly polarized light, the measured angular distributions can be quantitatively examined by transforming the laboratory frame distributions by using $I(\theta) \sim 1 + \beta \cdot P_2(\cos \theta)$. Here, θ is the angle between the recoil direction and the polarization of the 355 nm pump laser, and P_2 is a second-order Legendre polynomial. Using the pBASEX³⁰ program, 3D image reconstruction extracts the anisotropy parameter β . Overall, the anisotropy parameter across the main feature in each ion image is slightly negative but effectively zero and does not change over the kinetic energies observed, confirming that the angular distributions are isotropic. Note that these results support a picture of NO dissociation occurring after the molecule undergoes electronic relaxation from S_1 to a lower-lying electronic state as opposed to rapid dissociation on the S_1 state.

Furthermore, the ion images were analyzed with pBASEX³⁰ to determine the velocity distributions of the NO ($\nu'' = 0, J''$) products. This is accomplished by implementing an inverse Abel transformation along the vertical axis and subsequently

integrating the radial distributions over the polar angle. Using conservation of momentum, the total kinetic energy released (TKER) to NO + aromatic radical products are obtained. The resulting TKER distributions for the $Q_1(J'')$ and $R_1(J'')$ rotational levels are shown in Figures 2–4 for nitrobenzene, *o*-nitrophenol, and 2-nitroresorcinol, respectively. The TKER distributions for nitrobenzene and *o*-nitrophenol are broad, extending over 8000 cm^{-1} with breadths of 4650 cm^{-1} across the full width at half-maximum. Conversely, the TKER distributions from 2-nitroresorcinol photolysis span to 12 000 cm^{-1} with the full width at half-maximum $\sim 4500 \text{ cm}^{-1}$. Furthermore, the average energy placed into translation is $\langle \text{TKER} \rangle \sim 3300 \text{ cm}^{-1}$ from fragmentation of nitrobenzene and *o*-nitrophenol, and approximately 3780 cm^{-1} for 2-nitroresorcinol. Though a full energy partitioning study was not carried out, the energy channeled to product recoil velocity probed at different NO rotational levels in $\nu'' = 0$ is approximately 15% of the available energy. Galloway et al. explored the average kinetic energies for photodissociation of nitrobenzene to NO + phenoxy from 220 to 320 nm and showed that the translational energy comprised about 20% of the available energy at all photolysis wavelengths.¹⁵ The present results are in excellent agreement with this previous study, despite exciting nitrobenzene to a different electronic state.

To further analyze the experimental TKER data, a Prior distribution is employed to predict the energy partitioning to the relative recoil velocity between the NO + aromatic cofragments for comparison with the TKER distributions. A Prior distribution is a statistical method based on the

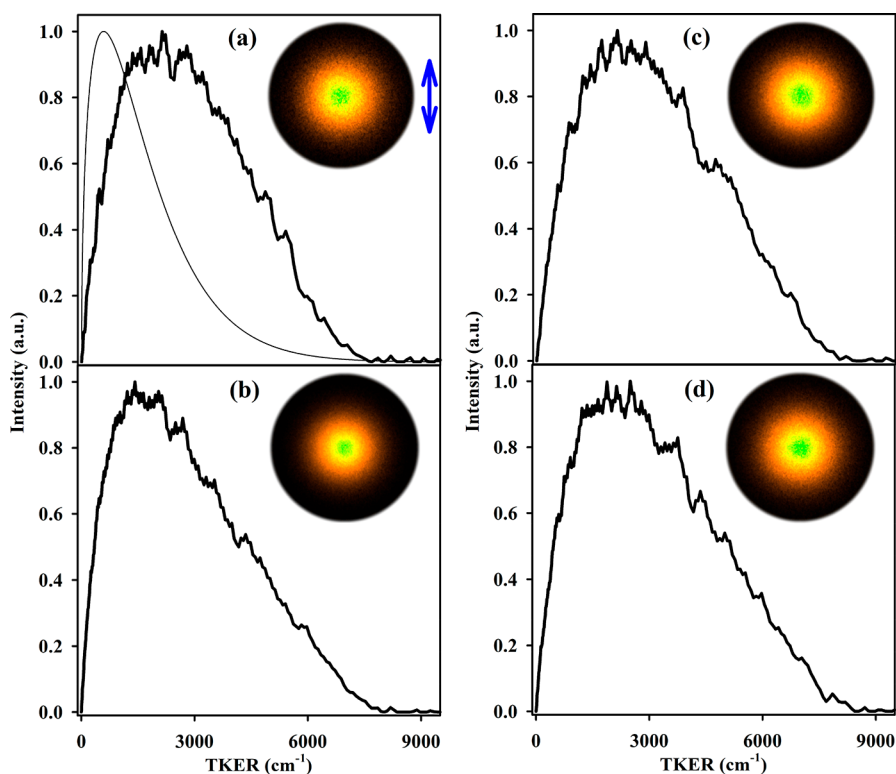


Figure 3. Velocity map ion images of NO products and total kinetic energy release (TKER) to NO ($\nu'' = 0$) and hydroxyphenoxy products (black bold traces) recorded by using the (a) $Q_1(J''=20.5)$, (b) $R_1(J''=20.5)$, (c) $Q_1(J''=30.5)$, and (d) $R_1(J''=30.5)$ transitions following 355 nm photolysis of *o*-nitrophenol using vertical polarization (blue arrow). The statistical Prior distribution (nonbold trace) is superimposed over the experimental results in the upper left panel.

assumption that, without dynamical bias, all final quantum states of products are equally likely to be populated.⁴⁴ Therefore, all energetically available product quantum states up to the available energy must be determined. The quantum states are then partitioned into groups on the basis of the resolution of the experiment. The groups with a greater number of states will have a larger population since all quantum states have an equal probability to be occupied, thus creating a nonuniform distribution. Only the quantum states for the aromatic radical are included in the state count since the quantum state of NO $X^2\Pi_{1/2}$ ($\nu'' = 0$, $Q_1(J'')$) or ($\nu'' = 0$, $R_1(J'')$) is fixed during the experiment ($E_{\text{int}}(\text{NO})$). Therefore, the energy E released to products is decreased by the fixed NO internal energy to

$$E = E_{\text{avl}} - E_{\text{int}}(\text{NO}) \quad (1)$$

We define E_{avl} to be the available energy to the NO + aromatic cofragment products and to be equivalent to the UV excitation energy minus the computed reaction endothermicity,

$$E_{\text{avl}} = E_{h\nu} - \Delta E_{\text{rxn}} \quad (2)$$

Here, ΔE_{rxn} is the energy difference between the parent nitroaromatic stationary points and their corresponding products. Therefore, $\Delta E_{\text{rxn}} = 6010 \text{ cm}^{-1}$ for nitrobenzene, $\Delta E_{\text{rxn}} = 4400 \text{ cm}^{-1}$ for *o*-nitrophenol, and $\Delta E_{\text{rxn}} = 2140 \text{ cm}^{-1}$ for 2-nitroresorcinol on the basis of the MRMPT2 calculations described below. The expression for the density of translational states is

$$\rho(E_T) = A_T g(E_{\text{int}}(\text{aromatic}))(E_T - E_{\text{int}}(\text{aromatic}))^{1/2} \quad (3)$$

where E_T is the translational energy, $E_{\text{int}}(\text{aromatic})$ is the internal energy of the aromatic cofragment, $g(E_{\text{int}}(\text{aromatic}))$ is the degeneracy of the aromatic cofragment at $E_{\text{int}}(\text{aromatic})$, and A_T is a normalization constant. The total density of states $\rho(E)$ at the energy E is the sum of $\rho(E_T)$ over all internal rovibrational states of the aromatic cofragment that are allowed by conservation of energy. The Prior distribution for translational energy is then calculated as $P(E_T) = \rho(E_T)/\rho(E)$. The Prior distribution is straightforward to implement, yet it has several limitations.⁴⁵ However, this method may be used to ascertain a deviation of the experimental results from a statistical distribution of energy after photolysis, which reflects dynamical constraints in the photodissociation process.

The results derived from the Prior calculations are plotted as nonbold traces on the experimental TKER distributions in Figures 2–4. To determine the accessible aromatic radical quantum states required in the Prior simulations, available rotational constants were obtained from microwave spectroscopy,^{42,43} and the rotational constants of the 2,6-dihydroxyphenoxy radical were obtained from calculations. The calculated anharmonic frequencies in the Supporting Information provided the vibrational level energies. Additionally, the hydroxyl group torsions were treated as harmonic oscillators for the Prior calculations carried out for *o*-nitrophenol and 2-nitroresorcinol photodissociation. The most probable translational energy from the simulated Prior distributions for nitrobenzene and *o*-nitrophenol is approximately 600 cm^{-1} , whereas the most probable value is $\sim 520 \text{ cm}^{-1}$ for 2-nitroresorcinol. Additionally, the predicted average translational energy from nitrobenzene, *o*-nitrophenol, and 2-nitroresorcinol dissociation is 1680, 1640, and 1610 cm^{-1} ,

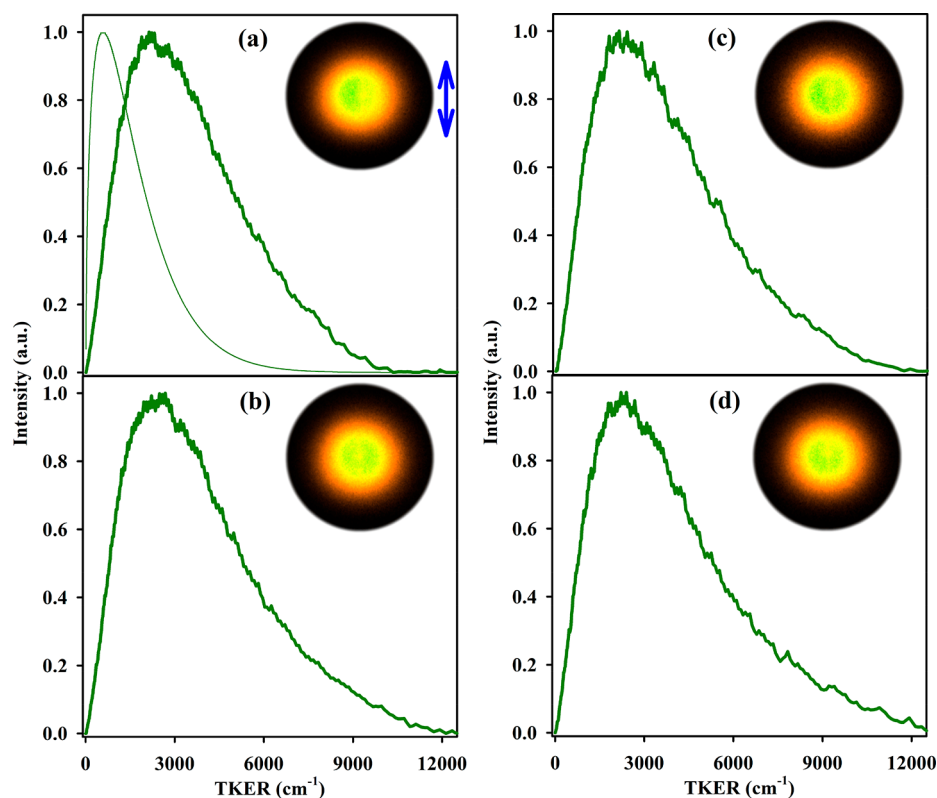


Figure 4. Velocity map ion images of NO products and total kinetic energy release (TKER) to NO ($\nu'' = 0$) and dihydroxyphenoxy products (green bold traces) recorded by using the (a) $Q_1(J''=25.5)$, (b) $R_1(J''=25.5)$, (c) $Q_1(J''=35.5)$, and (d) $R_1(J''=35.5)$ transitions following 355 nm photolysis of 2-nitroresorcinol using vertical polarization (blue arrow). The statistical Prior distribution (nonbold trace) is superimposed over the experimental results in the upper left panel.

respectively. Overall, the Prior calculations predict TKER distributions that differ significantly from the experimental results, indicating that the distribution of energy upon photodissociation is considerably nonstatistical.

NO product state distributions following 355 nm photolysis of nitrobenzene, *o*-nitrophenol, and 2-nitroresorcinol were recorded by probing selected $Q_1(J'')$ and $R_1(J'')$ transitions in the $A^2\Sigma^+ \leftarrow X^2\Pi(0,0)$ band system. Each probe transition is scanned three times, and the monitored signal intensity is integrated and divided by the state degeneracy factor ($2J'' + 1$), probe pulse energy, and the line strength from LIFBASE²⁹ to obtain the population of the individual states. The natural logarithm of the population for each probed R-branch rotational level $P(J'')/(2J'' + 1)$ is plotted against the internal energy of NO ($\nu'' = 0, J''$) denoted as $E_{\text{int}}(\text{NO})$ in Figure 5. The Supporting Information shows both Q- and R-branch rotational state distribution results. The slope is obtained from the fit to the experimental data to extract a rotational temperature (T_{rot}) for the $Q_1(J'')$ and $R_1(J'')$ branches, assuming a Boltzmann rotational distribution. The T_{rot} therefore serves as a measure of the rotational excitation. We note that there is no reason that the product state distributions should assume a specific rotational temperature, but the results may be used to explore rotational populations following photolysis and Λ -doublet state propensities. In particular, the Q-branch transitions have a high selectivity for the $\Pi(A'')$ state, whereas the $\Pi(A')$ state may be probed with the R-branch (or P-branch) transitions.⁴⁶

Prior simulations were also carried out to predict the NO product state distributions in $\nu'' = 0$ from photolysis of

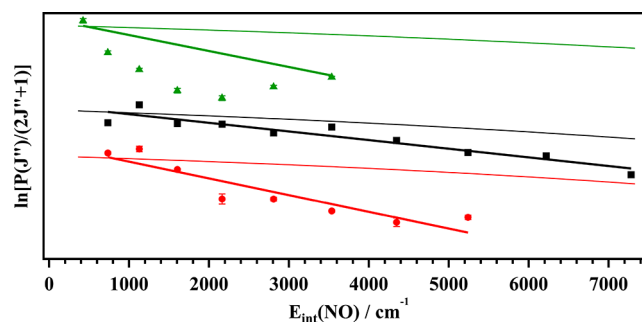


Figure 5. Product state distributions of NO $X^2\Pi(\nu'' = 0, J'')$ products for the R-branch from the 355 nm photolysis of nitrobenzene (red circles), *o*-nitrophenol (black squares), and 2-nitroresorcinol (green triangles). The NO populations for the R-branch are fitted to a Boltzmann distribution (bold traces), and the Prior simulation results are overlaid on the experimental data as nonbold traces. Note that the NO product state distributions have been vertically displaced from one another to emphasize their differences.

nitrobenzene, *o*-nitrophenol, and 2-nitroresorcinol. Similar to the discussion above, E_{avl} was fixed and the accessible energy levels of NO and the aromatic cofragments were determined. Next, the relative populations, which are proportional to their density of states $\rho(E_{\text{int}}(\text{NO}))$ and $\rho(E_{\text{int}}(\text{aromatic}))$, were calculated. Furthermore, each energetically accessible pair of NO and aromatic radical product levels is weighted by their respective rovibronic degeneracies and also weighted by their translational density of states, $\rho(E_T)$.

The experimental T_{rot} of the Q- and R-branches are 3400 ± 500 and 3400 ± 600 K, respectively, for NO from

nitrobenzene decomposition. Conversely, the experimental T_{rot} is 6000 ± 1000 K for the Q-branch and 6600 ± 800 K for the R-branch manifold from *o*-nitrophenol photolysis at 355 nm. Thus, the distributions reveal that both Λ -doublet levels are equally populated within experimental uncertainty. However, the average T_{rot} of NO products is a factor of 2 larger from *o*-nitrophenol photolysis compared to that for nitrobenzene and 2-nitroresorcinol. The NO product state distribution obtained from 2-nitroresorcinol photolysis is particularly intriguing since it is clearly nonlinear, signifying a non-Boltzmann rotational distribution. Therefore, the T_{rot} obtained for NO from 2-nitroresorcinol photolysis (4000 ± 2000 K) by using a Boltzmann distribution is qualitative at best. As Figure 5 shows, the population of higher-energy NO rotational states is less from 2-nitroresorcinol dissociation compared to the other systems. In any event, a significant deviation is evident in comparing the experimental NO product state distributions (bold traces) in Figure 5 to the Prior simulation results (nonbold traces), further revealing nonstatistical behavior. It should be noted that the NO product state distributions in Figure 5 have been displaced from one another to emphasize their differences.

The S_0 and T_1 (16,13) MRMPT2/aug-cc-pVDZ// (14,11) MCSCF/aug-cc-pVDZ PESs for nitrobenzene calculated in this study are shown in Figure 6. On S_0 , a large barrier (64.4

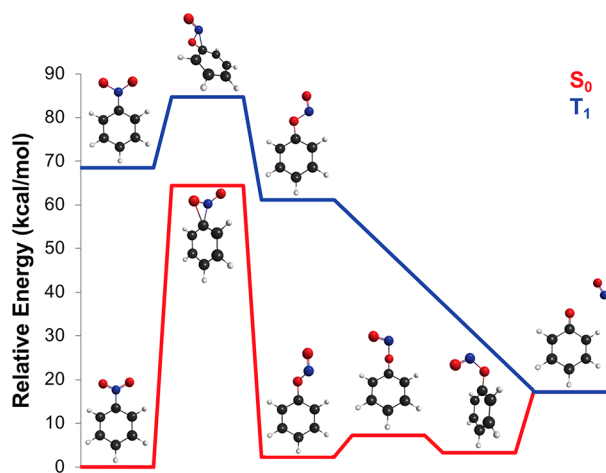


Figure 6. Schematic S_0 and T_1 potential energy surfaces for nitrobenzene calculated at the (16,13) MRMPT2/aug-cc-pVDZ// (14,11) MCSCF/aug-cc-pVDZ level of theory along with the stationary point geometries.

kcal/mol) separates nitrobenzene from the nearly isoenergetic phenyl nitrite isomer. The two conformational isomers of phenyl nitrite, which are separated by a relatively small barrier, can both undergo endothermic decomposition to yield NO and phenoxy. On the T_1 PES, the barrier for isomerization from nitrobenzene to phenyl nitrite is significantly smaller (16.2 kcal/mol) and the isomerization is energetically favorable by 7.3 kcal/mol. The barrierless decomposition of phenyl nitrite into NO and phenoxy is strongly exothermic on T_1 .

The PESs shown in Figure 6 are in generally good agreement with the G2M(CC1)//UB3LYP/6-311+G(3df,2p) PESs reported in Hause et al.¹⁸ The PESs reported in the present work were obtained by using multireference approaches with large active spaces, albeit with a relatively modest aug-cc-pVDZ basis, whereas Hause et al. used a

composite, single-reference approach to obtain the electronic energy at DFT optimized geometries. One notable difference between the two PESs is that we were unable to identify a NO_2 roaming transition state geometry on S_0 despite trying multiple starting geometries, including a structure with C–N and C–O distances consistent with the values reported in ref 18. It is worth noting that Hause et al. reported that their roaming transition state calculations displayed spin-contamination as well as evidence of significant multireference character.

The S_0 (18,14) MRMPT2/aug-cc-pVDZ// (18,14) MCSCF/aug-cc-pVDZ PES for the *syn* conformer of *o*-nitrophenol calculated in this study is shown in Figure 7.

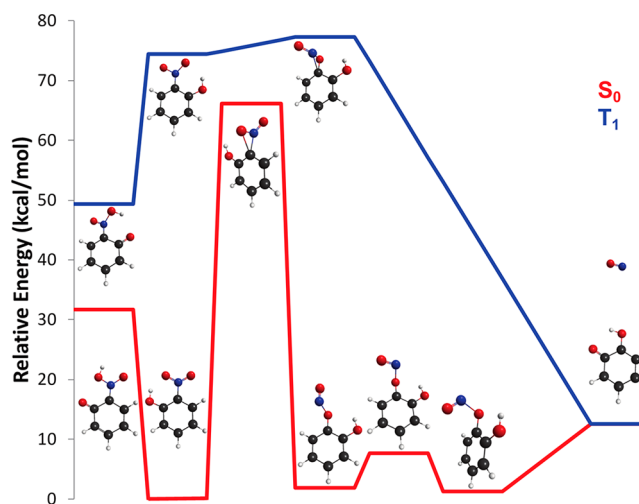


Figure 7. Schematic S_0 and T_1 potential energy surfaces for the *syn* conformer of *o*-nitrophenol calculated at the (18,14) MRMPT2/aug-cc-pVDZ// (18,14) MCSCF/aug-cc-pVDZ level of theory along with the key stationary point geometries.

Similar to nitrobenzene, the nearly isoenergetic *o*-nitrophenol and *o*-hydroxyphenyl nitrite isomers are separated by a large, 66.1 kcal/mol barrier. The two conformations of *o*-hydroxyphenyl nitrite are separated by a relatively small 5.8 kcal/mol barrier and can both undergo endothermic decomposition to yield NO and *o*-hydroxyphenoxy. Proton transfer from the hydroxyl to the nitro group is uphill in energy by 31.6 kcal/mol. Finally, as shown in the Supporting Information, a similar pattern of S_0 stationary points is observed for the higher-energy *anti* conformer. It is worth noting that the *anti* conformer is 11.4 kcal/mol higher in energy than the *syn* conformer, a result of the nitro group losing both hydrogen bonding and π -conjugation; the minimum energy geometry of the *anti* conformer has the nitro group rotated significantly out of plane.

The T_1 PES for the *syn* conformer of *o*-nitrophenol is also shown in Figure 7 whereas the corresponding data for the *anti* conformer is reported in the Supporting Information. In contrast with the S_0 PES, proton transfer from the hydroxyl to the nitro group is exothermic by 24.9 kcal/mol. Unlike nitrobenzene, we were unable to identify an *o*-hydroxyphenyl nitrite minimum energy stationary point geometry on T_1 . Instead, a low 2.9 kcal/mol barrier separates *o*-nitrophenol from a strongly exothermic (61.8 kcal/mol) decomposition into NO and hydroxyphenoxy.

The S_0 (18,14) MRMPT2/aug-cc-pVDZ// (18,14) MCSCF/aug-cc-pVDZ PES for the *syn-syn* conformer of

2-nitroresorcinol calculated in this study is shown in Figure 8. Similar to results for nitrobenzene and *o*-nitrophenol, a large

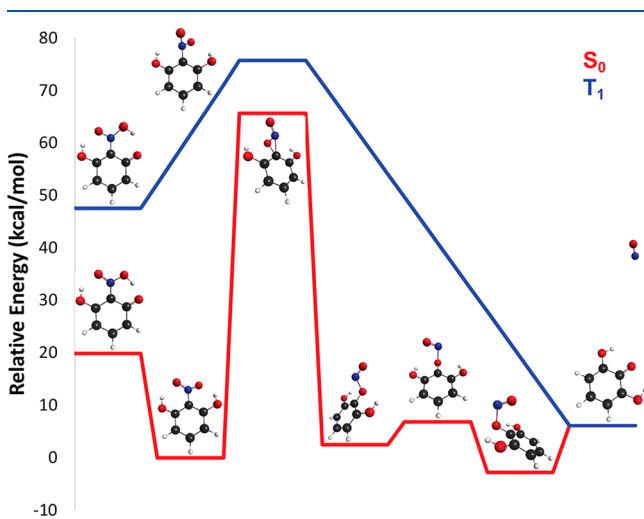


Figure 8. Schematic S_0 and T_1 potential energy surfaces for the *syn-syn* conformer of 2-nitroresorcinol calculated at the (18,14) MRMP2/aug-cc-pVDZ// (18,14) MCSCF/aug-cc-pVDZ level of theory along with the key stationary point geometries.

65.6 kcal/mol barrier separates the 2-nitroresorcinol and dihydroxyphenyl nitrite isomers. Unlike the other two compounds, one of the dihydroxyphenyl nitrite conformers is 2.8 kcal/mol lower in energy than 2-nitroresorcinol. The two dihydroxyphenyl nitrite conformers can both undergo endothermic decomposition and are separated by a relatively low 4.3 kcal/mol barrier. Proton transfer from one of the hydroxyl groups to the nitro group is uphill in energy by 19.8 kcal/mol. Similar to *o*-nitrophenol, the *anti-anti* conformer of 2-nitroresorcinol is higher in energy than the *syn-syn* conformer by 11.0 kcal/mol due to the nitro group being distorted out of plane. As shown in the Supporting Information, the pattern of S_0 stationary points for the *anti-anti* conformer of 2-nitroresorcinol is similar to those of the *syn-syn* conformer. Finally, it is worth noting that the decomposition on S_0 becomes decreasingly endothermic with each additional hydroxyl group; for the *syn* conformers, the decomposition into NO and aromatic cofragment has $\Delta E = 17.2$ kcal/mol for nitrobenzene, $\Delta E = 12.6$ kcal/mol for *o*-nitrophenol, and $\Delta E = 6.1$ kcal/mol for 2-nitroresorcinol.

The T_1 PES for the *syn-syn* conformer of 2-nitroresorcinol is also shown in Figure 8 whereas the corresponding data for the *anti-anti* conformer are reported in the Supporting Information. Note that the optimized geometry of 2-nitroresorcinol on T_1 includes a significant out of plane distortion of the nitro group. Similar to the case for *o*-nitrophenol, proton transfer from the hydroxyl to the nitro group is exothermic by 28.2 kcal/mol on T_1 . Also like *o*-nitrophenol, stable dihydroxyphenyl nitrite minima were not observed on the T_1 PES. Decomposition to NO and dihydroxyphenoxy was found to be exothermic by 69.6 kcal/mol. While a barrier preceding dissociation was not identified for the *syn-syn* conformer, a small 2.3 kcal/mol barrier was found for the *anti-anti* conformer.

5. DISCUSSION

Hause¹⁸ reported on the 226 nm photolysis of nitrobenzene, presenting ion images with a bimodal translational distribution as a function of the probed NO rotational state J'' . For low J'' , only a slow component is present, but with increasing J'' , the faster translational component appears. Consistent with Figure 6, the faster component was ascribed to NO production from the T_1 triplet state surface, where the strong exothermicity of dissociation would impart significant translational energy to the fragments. The slower component was assigned to fragmentation occurring on the ground state PES, where dissociation is uphill in energy from phenyl nitrite. Using energy-dependent branching ratio calculations, Hause et al. argued further that the slow component was specifically due to a roaming pathway on S_0 . We reproduce the slow and fast components in ion images for nitrobenzene photolysis at 226 nm. In a future publication, we will describe the 226 nm photodissociation dynamics of *o*-nitrophenol and 2-nitroresorcinol to NO products.⁴⁷

For the present study, focusing on the 355 nm photodissociation of nitrobenzene, only the slow component is evident in all ion images, even at high NO (J''). On the basis of the previous results by Hause as well as the PESs in Figure 6, this is consistent with the dissociation occurring on S_0 . While T_1 is not directly involved in the actual dissociation, the triplet manifold could certainly be involved in the electronic relaxation back to S_0 . In particular, the intersystem crossing pathway from the nitrobenzene minimum on T_1 to the phenyl nitrite minimum on S_0 reported by Giussani and Worth allows for a circumvention of the large isomerization barrier on S_0 .²⁵ Because we could not obtain a MCSCF optimized geometry for a NO₂ roaming transition state, along with the limitations Hause et al. reported in their calculations of this stationary point, it seems possible that the fragmentation on S_0 occurs through a nonroaming pathway. We cannot, however, definitively rule out a roaming mechanism without a more in-depth analysis, such as directly modeling the photodissociation dynamics.

Similarly, ion images obtained from *o*-nitrophenol and 2-nitroresorcinol 355 nm photodissociation only possess a single component regardless of the probed NO ($v'' = 0, J''$) level. Moreover, the TKER distributions for all three parent molecules are similar and are consistent with, on average, approximately 15% of the total available energy going into the translational motion of the fragments. Referring to the calculated surfaces, this suggests that dissociation of the three nitroaromatic chromophores occurs on the S_0 PES, where the O–NO bond cleavage is uphill in energy, as opposed to the T_1 PES, where the exothermicity of the dissociation would lead to larger translational energies.

The predicted translational distributions from 355 nm photodissociation of nitrobenzene, *o*-nitrophenol, and 2-nitroresorcinol were determined by using a statistical Prior calculation discussed in the previous section. The calculated average energy imparted to translation from nitrobenzene, *o*-nitrophenol, and 2-nitroresorcinol photolysis is 1680, 16400, and 1640 cm⁻¹, respectively. The Prior simulation results deviate substantially from the average TKER results observed in the experimental data, which indicates the presence of a dynamical constraint in the dissociation dynamics. More specifically, the experimental TKER distributions indicate that less energy is stored in the internal energy of the aromatic

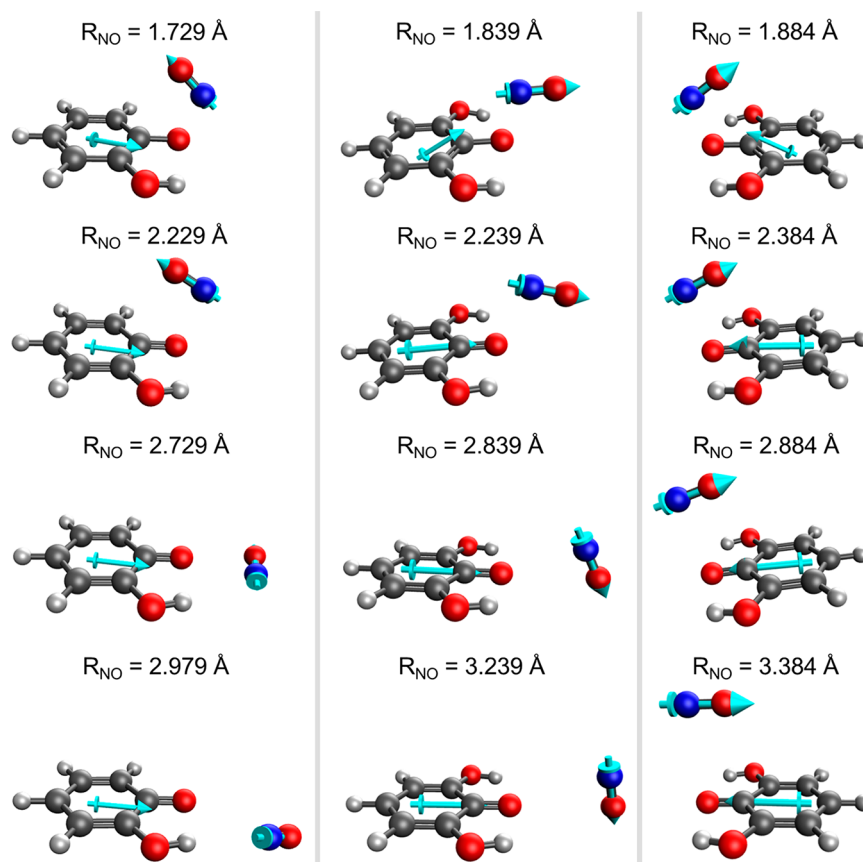


Figure 9. Representative geometries from MCSCF relaxed scans of *o*-nitrophenol (left column) and two isomers of 2-nitroresorcinol (middle and right columns) along the O–NO bond dissociation coordinate. The first geometry in all three scans is displaced 0.25 Å from the corresponding minimum energy geometry. The fragment dipole moments are shown superimposed on the molecular geometries, with the dipole moment of NO enlarged for clarity.

fragments than would be predicted on the basis of a purely statistical distribution of the energy among the various quantum states. As a result, a greater fraction of the available energy ends up in the translational energy of the fragments. Furthermore, the Prior simulations for the NO product state distributions indicate that less energy is partitioned to NO rotation in experiments. It is worth noting that statistical Prior simulations treat the radical cofragments as structureless and noninteracting, which can lead to considerable discrepancies when compared to experimental observations.

Figure 5 shows the results of the product state distribution obtained for the R-branches of NO from nitrobenzene, *o*-nitrophenol, and 2-nitroresorcinol photodissociation. Since these distributions are plotted as the logarithm of a Boltzmann distribution, written as $P(J'') \sim \exp[-E_{\text{int}}(J'')/kT_{\text{rot}}]$, versus the rotational energy level $E_{\text{int}}(\text{NO})$, the slope of the graphs yields the T_{rot} of the individual branches. For all parent nitroaromatic molecules, this analysis indicates that NO is formed with significant rotational excitation, albeit consistently less than what is predicted with statistical Prior simulations. Furthermore, production of NO from 2-nitroresorcinol photolysis results in a non-Boltzmann distribution of rotational states. It is to these deviations from statistical treatments that we now turn.

The results of MCSCF relaxed scans of one isomer of *o*-nitrophenol and two isomers of 2-nitroresorcinol along the O–NO dissociation coordinate are shown in Figure 9, beginning with geometries that are displaced by 0.25 Å from the

corresponding minimum energy geometry. Previous studies on the H atom abstraction reaction between chlorine (Cl) radicals and a variety of organic molecules described trends in the HCl product state distribution based on the chemical structure of the organic radical coproduct.^{48–51} Specifically, the extent of rotational excitation of the HCl was correlated with the magnitude and relative orientations of the fragment dipole moments at the transition state and product complex geometries. Influenced by this approach, the dipole moments of the radical fragments were calculated at each geometry in the scan and are shown superimposed on the molecular structures in Figure 9. The dipole moment of NO has been enlarged for clarity. The complete set of MCSCF relaxed scans can be found in the Supporting Information.

The middle and right columns of Figure 9 focus on two MCSCF relaxed scans of 2-nitroresorcinol. In the first of these scans (middle column), evidence of a significant torque on the dissociating NO fragment is clearly evident, with the NO nearly perpendicular to the aromatic plane in the final geometry. The presence of a reorientation of the NO group along this minimum energy dissociation path is consistent with significant rotational excitation of the dissociating NO fragment. Note that in this scan, the dipole moments of the two fragments are initially oriented head-to-tail (although vertically displaced from each other) and end up nearly perpendicular. In the second scan (right column), the dipole moments of the two fragments begin with a 115.4° angle between them and end nearly antiparallel to one another.

Along this minimum energy dissociation pathway, the NO experiences a much smaller torque, largely moving directly away from the aromatic cofragment.

It is worth noting that the trend observed in the middle and right columns of Figure 9 is counter to that observed in previous studies on H atom abstraction reactions. Specifically, in the previous studies, the less the alignment between the HCl and organic radical dipole moments at the transition state or product complex geometry, the greater the rotational excitation of the HCl molecule. This was rationalized through an electrostatic induced torque on the HCl that steers the products into a more favorable dipole moment alignment. In contrast, the relaxed scan in Figure 9 with the greatest torque induced on the NO begins with the fragment dipole moments nearly parallel to one another. However, unlike in the H atom abstraction reactions, the fragment dipole moments are significantly vertically displaced from each other. This vertical displacement between the dipole moments leads to a much more anisotropic potential than if the dipole moments were collinear, allowing for the torque observed in the relaxed scans.

As shown in the Supporting Information, analogous MCSCF relaxed scans for nitrobenzene are very similar to the 2-nitroresorcinol scans shown in Figure 9. The magnitudes of the dipole moments are significantly larger for nitrobenzene than for 2-nitroresorcinol. For example, at the first geometry in the center column in Figure 9 the dipole moments are 0.96 and 0.18 D for dihydroxyphenoxy and NO, respectively. In the corresponding MCSCF relaxed scan for nitrobenzene, the values are 2.65 and 0.21 D for phenoxy and NO. The larger dipole moments of the radical fragments of nitrobenzene will result in greater long-range dipole–dipole interactions, which may explain the population of higher NO(J'') states from nitrobenzene photodissociation as compared to that of 2-nitroresorcinol. Previous studies of H atom abstraction reactions of Cl with a range of organic molecules similarly correlated the T_{rot} of the HCl product with the dipole moment magnitude of the organic radical product.⁵¹

Turning to *o*-nitrophenol, the MCSCF relaxed scan in Figure 9 shows the presence of significant long-range interactions which steer the dissociating NO molecule into the plane of the aromatic fragment. As shown in the Supporting Information, this long-range movement of the NO molecule from being above the aromatic plane to being nearly coplanar with the hydroxyphenoxy fragment was observed in all of the calculated minimum energy dissociation pathways of *o*-nitrophenol, although the NO was not exclusively steered to the side of the molecule with the hydroxyl group. The asymmetric motion observed in the minimum energy NO dissociation pathways of *o*-nitrophenol reflects the asymmetric charge distribution of the hydroxyphenoxy fragment. The MCSCF relaxed scans suggest that in *o*-nitrophenol, the dissociating NO experiences a more complex set of anisotropic long-range forces than in the other two nitroaromatic species, giving rise to greater and more complex rotational motion. This is consistent with the experimental observation of a significantly higher NO T_{rot} from *o*-nitrophenol photolysis than from nitrobenzene or 2-nitroresorcinol photolysis.

The highly non-Boltzmann NO rotational distribution from the photolysis of 2-nitroresorcinol shown in Figure 5 merits additional discussion. Given the strong similarity between the MCSCF relaxed scans of nitrobenzene and 2-nitroresorcinol, the present analysis is insufficient to fully explain the

differences present in the NO rotational populations obtained from the photolysis of these two species. Instead, the non-Boltzmann NO rotational distribution of 2-nitroresorcinol photolysis likely reflects details of the nonradiative relaxation pathways that are operative after excitation to S_1 along with the specific molecular configurations on S_0 that these connect to. Additionally, the UV/visible spectrum of 2-nitroresorcinol shown in the Supporting Information suggests that 355 nm radiation may induce excitation to a higher-lying bright state in addition to S_1 . The involvement of a second bright state in the photodissociation process may provide another explanation for the marked difference in the NO product state distribution of 2-nitroresorcinol as compared to that of nitrobenzene and *o*-nitrophenol. However, the absence of bimodal VMI images and TKER distributions suggests that if a second bright state were involved in the 355 nm photolysis of 2-nitroresorcinol, it follows the same general photochemistry as S_1 . Further analysis of the photodissociation of 2-nitroresorcinol will be the subject of future investigation.

The MCSCF relaxed scans also provide some insights into potential dynamical constraints in the dissociation pathways, which prevent a statistical partitioning of energy among the vibrational modes of the fragments. For all three nitroaromatic systems, cleavage of the O–NO bond is accompanied by in-plane distortions of the aromatic cofragment. Specifically, significant distortions along the relaxed scan are observed in the C–O bond length associated with the breaking O–NO bond, C–C bond lengths, C–C–C bond angles, and C–C–H bond angles. This suggests that as the O–NO bond breaks, energy will more readily flow into the vibrational modes associated with these in-plane distortions than vibrational modes primarily involving out-of-plane distortions. As a result, a limited subset of the vibrational state density will be populated in the cofragment relative to a fully statistical energy partitioning. Similar results were observed in previous H atom photofragment translational spectroscopy on the photodissociation of heteroaromatics, where dynamical constraints on the dissociation pathway led to selective population of aromatic ring distortions.^{52,53}

6. CONCLUSION

The work described above represents the first investigation of the dynamics associated with the formation of NO from the photodissociation of nitrobenzene, *o*-nitrophenol, and 2-nitroresorcinol after 355 nm excitation. For all three nitroaromatics, velocity map imaging results point to relatively slow photolysis, leading to rotationally hot NO and significantly nonstatistical TKER and NO product state distributions. The slow time scale of the photolysis is attributed to the need for isomerization and nonradiative relaxation back to S_0 prior to the O–NO bond dissociation. The results of high-level theoretical calculations indicate the presence of long-range interactions between NO and the aromatic cofragment giving rise to a torque on the dissociating NO and hence the formation of rotationally hot NO. The deviations between the experimental TKER and NO product state distributions and the statistical Prior simulations indicate the presence of dynamical constraints on energy partitioning during the dissociation.

While there are similarities between the 355 nm photolysis of nitrobenzene, *o*-nitrophenol, and 2-nitroresorcinol, significant differences between the NO product state distributions of the three nitroaromatics suggest contrasting dissociation

processes giving rise to different nonstatistical photochemical dynamics. The computational analysis suggests that the NO experiences stronger and more anisotropic long-range interactions with hydroxyphenoxy than with the other two aromatic photofragments. This may explain why photolysis of *o*-nitrophenol produces NO with a rotational temperature that is twice that from nitrobenzene or 2-nitroresorcinol photolysis. The highly non-Boltzmann NO product state distribution observed following 2-nitroresorcinol photodissociation is an especially dramatic manifestation of nonstatistical energy partitioning in these systems and merits future studies capable of unraveling the detailed nonradiative pathways that 2-nitroresorcinol follows prior to dissociation on S_0 .

Nitroaromatics are important atmospheric molecules derived from anthropogenic and biogenic processes. Furthermore, they are known light-absorbing chromophores embedded in "brown carbon" (BrC) aerosols, giving rise to their enhanced absorption properties in the near-UV/visible regions. This study comprises a combined experimental and theoretical effort to examine the 355 nm solar photolysis of these three nitroaromatic chromophores that release NO upon fragmentation. Upon absorbing 355 nm solar radiation, each molecule is promoted to the S_1 electronic state followed by prompt de-excitation and dissociation on the S_0 ground electronic state. With a focus on obtaining a molecular-scale understanding of the fragmentation mechanisms following solar absorption, we report the nonstatistical signatures that are imprinted on the internal energies and relative recoil of products. A coherent picture emerges that is consistent with previous studies, which is that at atmospherically relevant solar wavelengths, non-radiative de-excitation from S_1 proceeds to S_0 , possibly through the T_n triplet manifold, followed by decomposition on S_0 . Though the NO formation channel may be comparatively low,¹⁰ the aromatic and NO radicals that are released from photolysis may enrich the molecular complexity in the particle phase and in the atmosphere. The studied nitroaromatics in the atmosphere will dissociate in the same manner as discussed in the present work. While thermal energy dissipation to the condensed phase may occur for nitroaromatics in aerosols, with photodecomposition may not be negligible. Therefore, results presented here provide insights to nitroaromatic chromophore dissociation to improve atmospheric models. Future work will focus on extending the wavelength photolysis range and exploring the dissociation dynamics of more complex nitroaromatic species implicated in BrC aerosols.

■ ASSOCIATED CONTENT

Supporting Information

The Supporting Information is available free of charge on the ACS Publications website at DOI: 10.1021/acs.jpca.9b02312.

UV/visible absorption spectra of *o*-nitrophenol and 2-nitroresorcinol, product state distributions of NO products for the Q- and R-branch branches, geometries from MCSCF relaxed scans, S_0 and T_1 potential energy surfaces, aromatic cofragments' harmonic vibrational frequencies, and active space molecular orbitals at representative optimized geometries (PDF)

■ AUTHOR INFORMATION

Corresponding Authors

*E-mail: apetit@fullerton.edu.

*E-mail: nmkidwell@wm.edu.

ORCID

Nathanael M. Kidwell: 0000-0002-7065-4486

Notes

The authors declare no competing financial interest.

■ ACKNOWLEDGMENTS

K.J.B., N.Q., W.E.F., R.T.K., A.K.A., L.M., and N.M.K. acknowledge funding from the NASA Virginia Space Grant Consortium New Investigator Award (Grant 17-223-100527-010) and funding from the Jeffress Trust Awards Program in Interdisciplinary Research. B.O., M.M., G.G.V., J.G., Z.S., and A.S.P. acknowledge startup funding from California State University, Fullerton, as well as computational support from the Center for Computational and Applied Mathematics. We gratefully acknowledge Emma Walhout and Rachel E. O'Brien for assisting us with the UV/visible spectra for *o*-nitrophenol and 2-nitroresorcinol.

■ REFERENCES

- (1) Lelieveld, J.; Evans, J. S.; Fnais, M.; Giannadaki, D.; Pozzer, A. The Contribution of Outdoor Air Pollution Sources to Premature Mortality on a Global Scale. *Nature* **2015**, *525*, 367–371.
- (2) *Climate Change 2014: Synthesis Report. Contribution of Working Groups I, II and III to the Fifth Assessment Report of the Intergovernmental Panel on Climate Change*; Pachauri, R. K., Meyer, L. A., Eds.; IPCC: Geneva, Switzerland, 2014.
- (3) Lin, P.; Liu, J.; Shilling, J. E.; Kathmann, S. M.; Laskin, J.; Laskin, A. Molecular Characterization of Brown Carbon (BrC) Chromophores in Secondary Organic Aerosol Generated from Photooxidation of Toluene. *Phys. Chem. Chem. Phys.* **2015**, *17*, 23312–23325.
- (4) Lin, P.; Aiona, P. K.; Li, Y.; Shiraiwa, M.; Laskin, J.; Nizkorodov, S. A.; Laskin, A. Molecular Characterization of Brown Carbon in Biomass Burning Aerosol Particles. *Environ. Sci. Technol.* **2016**, *50*, 11815–11824.
- (5) Bond, T. C. Spectral Dependence of Visible Light Absorption by Carbonaceous Particles Emitted from Coal Combustion. *Geophys. Res. Lett.* **2001**, *28*, 4075–4078.
- (6) Saleh, R.; Robinson, E. S.; Tkacik, D. S.; Ahern, A. T.; Liu, S.; Aiken, A. C.; Sullivan, R. C.; Presto, A. A.; Dubey, M. K.; Yokelson, R. J.; Donahue, N. M.; Robinson, A. L. Brownness of Organics in Aerosols from Biomass Burning Linked to their Black Carbon Content. *Nat. Geosci.* **2014**, *7*, 647–650.
- (7) Jacobson, M. Z. Isolating Nitrated and Aromatic Aerosols and Nitrated Aromatic Gases as Sources of Ultraviolet Light Absorption. *J. Geophys. Res.: Atmos.* **1999**, *104*, 3527–3542.
- (8) Laskin, A.; Laskin, J.; Nizkorodov, S. A. Chemistry of Atmospheric Brown Carbon. *Chem. Rev.* **2015**, *115*, 4335–4382.
- (9) Chen, J.; Wenger, J. C.; Venables, D. S. Near-Ultraviolet Absorption Cross Sections of Nitrophenols and Their Potential Influence on Tropospheric Oxidation Capacity. *J. Phys. Chem. A* **2011**, *115*, 12235–12242.
- (10) Sangwan, M.; Zhu, L. Absorption Cross Sections of 2-Nitrophenol in the 295–400 nm Region and Photolysis of 2-Nitrophenol at 308 and 351 nm. *J. Phys. Chem. A* **2016**, *120*, 9958–9967.
- (11) Frosig, L.; Nielsen, O. J.; Bilde, M.; Wallington, T. J.; Orlando, J. J.; Tyndall, G. S. Kinetics and Mechanism of the Reaction of Cl Atoms with Nitrobenzene. *J. Phys. Chem. A* **2000**, *104*, 11328–11331.
- (12) Feng, Y.; Ramanathan, V.; Kotamarthi, V. R. Brown Carbon: A Significant Atmospheric Absorber of Solar Radiation? *Atmos. Chem. Phys.* **2013**, *13*, 8607–8621.
- (13) Finlayson-Pitts, B. J.; Pitts, J. N. *Chemistry of the Upper and Lower Atmosphere*; Academic Press: San Diego, 2000.
- (14) Seinfeld, J. H.; Pandis, S. N. *Atmospheric Chemistry and Physics: From Air Pollution to Climate Change*, 3rd ed.; Wiley: New York, 2016.

- (15) Galloway, D. B.; Bartz, J. A.; Huey, L. G.; Crim, F. F. Pathways and Kinetic-Energy Disposal in the Photodissociation of Nitrobenzene. *J. Chem. Phys.* **1993**, *98*, 2107–2114.
- (16) Galloway, D. B.; Glenewinkelmeier, T.; Bartz, J. A.; Huey, L. G.; Crim, F. F. The Kinetic and Internal Energy of NO from the Photodissociation of Nitrobenzene. *J. Chem. Phys.* **1994**, *100*, 1946–1952.
- (17) Lin, M. F.; Lee, Y. T.; Ni, C. K.; Xu, S. C.; Lin, M. C. Photodissociation Dynamics of Nitrobenzene and *o*-Nitrotoluene. *J. Chem. Phys.* **2007**, *126*, 064310.
- (18) Hause, M. L.; Herath, N.; Zhu, R. S.; Lin, M. C.; Suits, A. G. Roaming-Mediated Isomerization in the Photodissociation of Nitrobenzene. *Nat. Chem.* **2011**, *3*, 932–937.
- (19) Cheng, S. B.; Zhou, C. H.; Yin, H. M.; Sun, J. L.; Han, K. L. OH produced from *o*-Nitrophenol Photolysis: A Combined Experimental and Theoretical Investigation. *J. Chem. Phys.* **2009**, *130*, 234311.
- (20) Grygoryeva, K.; Kubecka, J.; Pysanenko, A.; Lengyel, J.; Slavicek, P.; Farnik, M. Photochemistry of Nitrophenol Molecules and Clusters: Intra- vs Intermolecular Hydrogen Bond Dynamics. *J. Phys. Chem. A* **2016**, *120*, 4139–4146.
- (21) Ernst, H. A.; Wolf, T. J. A.; Schalk, O.; Gonzalez-Garcia, N.; Boguslavskiy, A. E.; Stolow, A.; Olzmann, M.; Unterreiner, A. N. Ultrafast Dynamics of *o*-Nitrophenol: An Experimental and Theoretical Study. *J. Phys. Chem. A* **2015**, *119*, 9225–9235.
- (22) Xu, C.; Yu, L.; Zhu, C. Y.; Yu, J. G. Photoisomerization Reaction Mechanisms of *o*-Nitrophenol Revealed by Analyzing Intersystem Crossing Network at the MRCI Level. *J. Phys. Chem. A* **2015**, *119*, 10441–10450.
- (23) Takezaki, M.; Hirota, N.; Terazima, M.; Sato, H.; Nakajima, T.; Kato, S. Geometries and Energies of Nitrobenzene Studied by CASSCF calculations. *J. Phys. Chem. A* **1997**, *101*, S190–S195.
- (24) Xu, S. C.; Lin, M. C. Computational Study on the Kinetics and Mechanism for the Unimolecular Decomposition of C₆H₅NO₂ and the Related C₆H₅+NO₂ and C₆H₅O+NO Reactions. *J. Phys. Chem. B* **2005**, *109*, 8367–8373.
- (25) Giussani, A.; Worth, G. A. Insights into the Complex Photophysics and Photochemistry of the Simplest Nitroaromatic Compound: A CASPT2//CASSCF Study on Nitrobenzene. *J. Chem. Theory Comput.* **2017**, *13*, 2777–2788.
- (26) Vereecken, L.; Chakravarty, H. K.; Bohn, B.; Lelieveld, J. Theoretical Study on the Formation of H- and O-Atoms, HONO, OH, NO, and NO₂ from the Lowest Lying Singlet and Triplet States in *ortho*-Nitrophenol Photolysis. *Int. J. Chem. Kinet.* **2016**, *48*, 785–795.
- (27) Mewes, J. M.; Jovanovic, V.; Marian, C. M.; Dreuw, A. On the Molecular Mechanism of Non-radiative Decay of Nitrobenzene and the Unforeseen Challenges this Simple Molecule Holds for Electronic Structure Theory. *Phys. Chem. Chem. Phys.* **2014**, *16*, 12393–12406.
- (28) Pan, C.; Zhang, Y.; Lee, J. D.; Kidwell, N. M. Imaging the Dynamics of CH₂Br Photodissociation in the Near Ultraviolet Region. *J. Phys. Chem. A* **2018**, *122*, 3728–3734.
- (29) Luque, J.; Crosley, D. R.; *LIFBASE*, 2.1.1 ed.; SRI International: Menlo Park, CA, 2013.
- (30) Dribinski, V.; Ossadtchi, A.; Mandelshtam, V. A.; Reisler, H. Reconstruction of Abel Transformable Images: The Gaussian Basis-Set Expansion Abel Transform Method. *Rev. Sci. Instrum.* **2002**, *73*, 2634–2642.
- (31) Schmidt, M. W.; Gordon, M. S. The Construction and Interpretation of MCSCF Wavefunctions. *Annu. Rev. Phys. Chem.* **1998**, *49*, 233–266.
- (32) Szalay, P. G.; Muller, T.; Gidofalvi, G.; Lischka, H.; Shepard, R. Multiconfiguration Self-Consistent Field and Multireference Configuration Interaction Methods and Applications. *Chem. Rev.* **2012**, *112*, 108–181.
- (33) Hirao, K. Multireference Møller-Plesset Method. *Chem. Phys. Lett.* **1992**, *190*, 374–380.
- (34) Schmidt, M. W.; Baldridge, K. K.; Boatz, J. A.; Elbert, S. T.; Gordon, M. S.; Jensen, J. H.; Koseki, S.; Matsunaga, N.; Nguyen, K. A.; Su, S. J.; Windus, T. L.; Dupuis, M.; Montgomery, J. A. General Atomic and Molecular Electronic-Structure System. *J. Comput. Chem.* **1993**, *14*, 1347–1363.
- (35) Gordon, M. S.; Schmid, M. W. *Advances in Electronic Structure Theory: GAMESS, A Decade Later*; Elsevier: Amsterdam, 2005; Chapter 41.
- (36) Bode, B. M.; Gordon, M. S. MacMolPlt: A Graphical User Interface for GAMESS. *J. Mol. Graphics Modell.* **1998**, *16*, 133–138.
- (37) Shao, Y. H.; Gan, Z. T.; Epifanovsky, E.; Gilbert, A. T. B.; Wormit, M.; Kussmann, J.; Lange, A. W.; Behn, A.; Deng, J.; et al. Advances in Molecular Quantum Chemistry Contained in the Q-Chem 4 Program Package. *Mol. Phys.* **2015**, *113*, 184–215.
- (38) Krylov, A. I. Equation-of-Motion Coupled-Cluster Methods for Open-Shell and Electronically Excited Species: The Hitchhiker's Guide to Fock Space. *Annu. Rev. Phys. Chem.* **2008**, *59*, 433–462.
- (39) Zhao, Y.; Truhlar, D. G. The M06 Suite of Density Functionals for Main Group Thermochemistry, Thermochemical Kinetics, Noncovalent Interactions, Excited States, and Transition Elements: Two New Functionals and Systematic Testing of Four M06-Class Functionals and 12 Other Functionals. *Theor. Chem. Acc.* **2008**, *120*, 215–241.
- (40) Barone, V. Anharmonic Vibrational Properties by a Fully Automated Second-Order Perturbative Approach. *J. Chem. Phys.* **2005**, *122*, 014108.
- (41) Frisch, M. J.; Trucks, G. W.; Schlegel, H. B.; Scuseria, G. E.; Robb, M. A.; Cheeseman, J. R.; et al. *Gaussian*; Gaussian, Inc.: Wallingford, CT, 2009.
- (42) Hernandez-Castillo, A. O.; Abeysekera, C.; Fritz, S. M.; Zwieter, T. S. Mass-Correlated CP-FTMW Spectroscopy: Structural Characterization of the Phenoxy Radical, submitted for publication.
- (43) Fritz, S. M.; Hays, B. M.; Hernandez-Castillo, A. O.; Abeysekera, C.; Zwieter, T. S. Multiplexed Characterization of Complex Gas-Phase Mixtures Combining Chirped-Pulse Fourier Transform Microwave Spectroscopy and VUV Photoionization Time-of-Flight Mass Spectrometry. *Rev. Sci. Instrum.* **2018**, *89*, 093101.
- (44) Levine, R. D. *Molecular Reaction Dynamics*; Cambridge University Press: Cambridge, 2009.
- (45) Baer, T.; Hase, W. L. *Unimolecular Reaction Dynamics: Theory and Experiments*; Oxford University Press, 1996.
- (46) Andresen, P.; Rothe, E. W. Analysis of Chemical-Dynamics Via Λ -Doubling - Directed Lobes in Product Molecules and Transition States. *J. Chem. Phys.* **1985**, *82*, 3634–3640.
- (47) Blackshaw, K. J.; Quartey, N. K.; Hood, D. J.; Belinda; Galvan, J.; Petit, A. S.; Kidwell, N. M. Velocity Map Imaging of NO Radical Products from UV Photodissociation of *ortho*-Nitrophenol and Nitroresorcinol, manuscript in preparation.
- (48) Rudic, S.; Murray, C.; Ascenzi, D.; Anderson, H.; Harvey, J. N.; Orr-Ewing, A. J. The Dynamics of Formation of HCl Products from the Reaction of Cl Atoms with Methanol, Ethanol, and Dimethyl Ether. *J. Chem. Phys.* **2002**, *117*, 5692–5706.
- (49) Rudic, S.; Murray, C.; Harvey, J. N.; Orr-Ewing, A. J. The Product Branching and Dynamics of the Reaction of Chlorine Atoms with Methylamine. *Phys. Chem. Chem. Phys.* **2003**, *5*, 1205–1212.
- (50) Rudic, S.; Murray, C.; Harvey, J. N.; Orr-Ewing, A. J. On-the-fly *ab initio* Trajectory Calculations of the Dynamics of Cl Atom Reactions with Methane, Ethane and Methanol. *J. Chem. Phys.* **2004**, *120*, 186–198.
- (51) Murray, C.; Pearce, J. K.; Rudic, S.; Retail, B.; Orr-Ewing, A. J. Stereodynamics of Chlorine Atom Reactions with Organic Molecules. *J. Phys. Chem. A* **2005**, *109*, 11093–11102.
- (52) Ashfold, M. N. R.; Cronin, B.; Devine, A. L.; Dixon, R. N.; Nix, M. G. D. The Role of $\pi\sigma^*$ Excited States in the Photodissociation of Heteroaromatic Molecules. *Science* **2006**, *312*, 1637–1640.
- (53) Ashfold, M. N. R.; Devine, A. L.; Dixon, R. N.; King, G. A.; Nix, M. G. D.; Oliver, T. A. A. Exploring Nuclear Motion through Conical Intersections in the UV Photodissociation of Phenols and Thiophenol. *Proc. Natl. Acad. Sci. U. S. A.* **2008**, *105*, 12701–12706.